Drift-aware sea ice thickness maps from satellite remote sensing

Robert Ricker[1], Thomas Lavergne[2], Stefan Hendricks[3], Stephan Paul[3], Emily Down[2], Mari Anne Killie[2], and Marion Bocquet[1]

[1]NORCE Norwegian Research Centre, Tromsø, Norway
[2]Norwegian Meteorological Institute, Oslo, Norway
[3]Alfred Wegener Institute, Helmholtz Centre for Polar and Marine Research, Bremerhaven, Germany

Correspondence: Robert Ricker (rori@norceresearch.no)

Abstract. The standard approach to deriving gridded sea ice thickness (SIT) from satellite altimeters is to aggregate the original along-track SIT estimates over a one-month period to achieve sufficient coverage across the Arctic. However, this approach neglects processes like sea ice advection, deformation, and thermodynamic growth that occur within the aggregation period. To address these limitations, we propose a drift-aware method that accounts for sea ice motion and SIT changes due to dynamics and thermodynamics in monthly SIT products. We present a method to derive daily drift-aware sea ice thickness (DA-SIT) maps for the Arctic, based on Envisat and CryoSat-2 along-track data. The approach is validated against buoys, airborne SIT surveys and moored upward-looking sonar (ULS) measurements. DA-SIT demonstrates the ability to register sea ice thickness anomalies, which are also observed by daily ULS SIT averages, while being overlooked by the conventional gridded SIT data. Comparative analysis reveals that drift-awareness reduces orbit track patterns in the gridded SIT and improves consistency in regions with significant ice drift, such as the Transpolar Drift. The drift-awareness facilitates detailed studies of regional sea ice dynamics and fluxes, while improving co-registration of multi-mission satellite data. However, when considering pan-Arctic estimates of ice volume, we do not expect significant changes in time series and trends compared to existing studies.

1 Introduction

The polar regions are a hot spot of climate change, associated with rising air temperatures (Landrum and Holland, 2020) and the transition of the Arctic Ocean to a state similar to Atlantic waters, a process known as Atlantification (Polyakov et al., 2017). As a consequence, Arctic sea ice significantly declined during the last decades, both in summer extent and year-round thickness (Comiso et al., 2008; Lindsay and Schweiger, 2015; Ricker et al., 2021). To monitor sea ice decline on a large scale, satellite observations are crucial. Observing sea ice thickness (SIT) is important as its magnitude regulates the heat exchange between ocean and atmosphere. In fact, SIT is an Essential Climate Variable (ECV) quantity (Lavergne et al., 2022) and critical to calculate sea ice volume and mass balance (Bocquet et al., 2024; Heorton et al., 2025) as well as fresh water fluxes (Ricker et al., 2018; Selyuzhenok et al., 2020).

Satellite altimetry has become the major tool for estimating SIT (Laxon et al., 2013; Ricker et al., 2014; Tilling et al., 2018; Petty et al., 2020). Within the European Space Agency (ESA) Climate Change Initiative (CCI), consistent SIT time series are developed across multiple satellite radar altimetry missions (ERS, Envisat, CryoSat-2, and Sentinel-3) to observe long-term

trends (Paul et al., 2018). However, existing methods for producing monthly SIT maps suffer from the fact that the sea ice is constantly in motion (Spreen et al., 2011), which is primarily driven by winds and, to a lesser extent, ocean currents. With the standard approach, along track SIT estimates derived from satellite altimetry measurements are typically collected over one month, allowing for an equal orbit coverage of the polar regions (Sallila et al., 2019). SIT is then averaged onto a fixed grid, where each input SIT estimate is geolocated at the time of the original measurement. Other methods use more advanced interpolation techniques, such as optimal interpolation or Bayesian approaches (Ricker et al., 2017; Gregory et al., 2021). All these approaches neglect sea ice drift occurring within the data collection period, and therefore introduces uncertainties in the final SIT maps. This is also important in the context of increasing sea ice drift speed over the last decades, and studies suggest that sea ice mobility will further increase in the future (Kwok et al., 2013; Zhang et al., 2022). Within the Transpolar Drift or Fram Strait, the geodesic displacement of sea ice can reach several 100 kilometers within a month (Kwok et al., 2004; Lavergne and Down, 2023). In addition to the advection of sea ice, deformation and thermodynamic ice growth occur within the data collection period of one month, meaning that SIT of a certain parcel derived in the beginning of a month will be altered by the end of the collection period. Moreover, because the temporal distribution of satellite orbits is uneven across regions throughout the month, the uncertainty associated with SIT changes will vary spatially.

As sea ice drift increases, advances in satellite altimetry, such as the laser altimeter on the NASA Ice, Cloud, and land Elevation Satellite 2 (ICESat-2), enable the detection of fine-scale features like individual sea ice pressure ridges (Farrell et al., 2020; Ricker et al., 2023). However, without accounting for sea ice motion, much of this detail can be lost when applying standard gridding techniques to generate SIT maps.

When retrieving geophysical information from multi-platform datasets, such as ice thickness from CryoSat-2 and The Soil Moisture and Ocean Salinity satellite (SMOS) (Ricker et al., 2017), correcting for ice motion prior to data merging is a step toward improving accuracy. Another example is the CRYO2ICE campaign (Fredensborg Hansen et al., 2024) to observe snow depth on sea ice by combining CryoSat-2 radar and ICESat-2 laser altimeter measurements, which currently relies on single-synchronized orbits due to sea ice drift.

To reduce uncertainties in SIT maps due to sea ice drift, we propose a novel approach that incorporates sea ice drift estimates from passive microwave satellite radiometers and combines them with satellite altimetry data to derive drift-aware sea ice thickness maps. This method allows individual parcels of satellite altimeter measurements to be advected over time, correcting for motion while also capturing sea ice thickness change as a consequence of thermodynamic growth and deformation effects between satellite overpasses.

Therefore our objective is to describe the drift-aware sea ice thickness (DA-SIT) algorithm, based on data from Envisat (2002-2012) and CryoSat-2 (2010-2020). In addition, our goal is to validate and benchmark DA-SIT using drifting buoys, airborne sea-ice thickness surveys and moored upward looking sonars (ULS), while assessing the impact of the drift-awareness algorithm by a comparison with conventionally gridded sea ice thickness products. In particular, we will show that neglecting sea ice drift causes significant spatial blurring and non-uniform temporal coverage in general, compromising the accuracy of regional thickness distributions

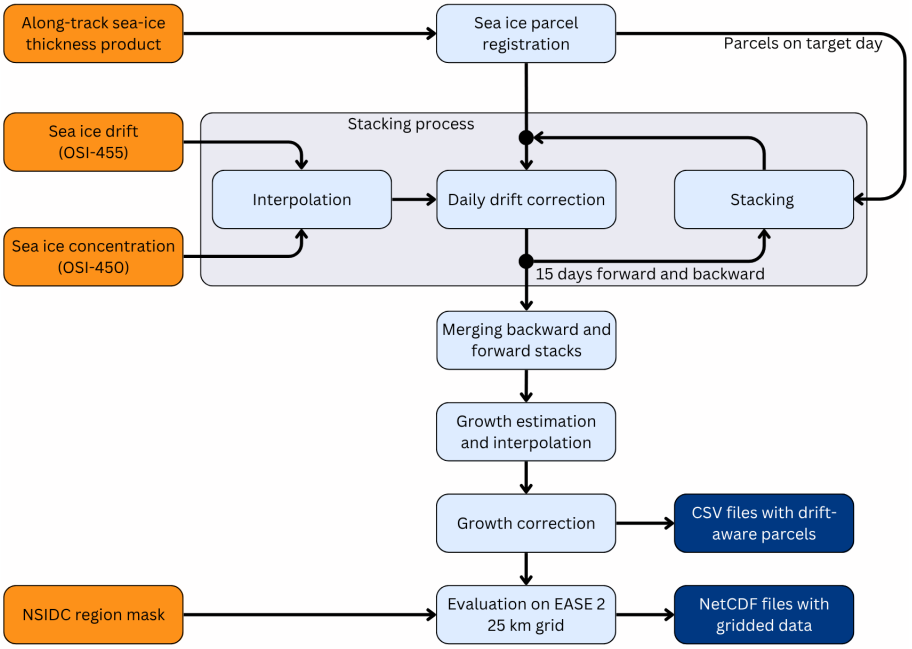

Figure 1. Drift-aware sea-ice thickness processing flow chart. Orange boxes indicate input data, light blue boxes indicate processes and dark blue boxes indicate output data products.

This paper is outlined as follows: in Section 2 in the first part, we describe the individual input data sets, while in the second part, we describe the drift-aware processing algorithm, including the associated uncertainty estimation. In Section 3, we present the results from the DA-SIT evaluation against independent validation datasets. In Section 4, we explore the impact of DA-SIT. Finally, conclusions are drawn in Section 5.

2 Data and Methods

2.1 Input Data

2.1.1 Altimeter Datasets

We have chosen to demonstrate the drift-awareness algorithm on SIT retrievals as they are most relevant for further scientific studies, but it is equally relevant for freeboard and other geophysical information obtained from altimetry.

As this study is related to the ESA CCI project, we use the latest CCI climate data record version 3.0 of SIT for the northern hemisphere polar region. The drift-awareness input altimetry data set contains the along-track geophysical variables including SIT and corresponding point-wise geolocation information (longitude, latitude), typically classified as level-2 datasets. Additional variables such as snow depth and freeboard are tracked along with the SIT data. The dataset includes two satellite missions. From October 2002 to March 2012, we use daily along track SIT data from the Radar Altimeter-2 (RA-2) instru-

ment on the Envisat satellite. From November 2010 to April 2020, we use daily SIT data from the SAR Interferometer Radar Altimeter (SIRAL) instrument aboard CryoSat-2. Both datasets cover the winter months (October to April) and are provided at full sensor resolution (Hendricks et al., 2024a, b).For a detailed description of the CCI along-track SIT retrieval processing, see Paul et al. (2024). This study is a proof-of-concept for single-altimeter data and in principle applicable to other platforms, such as ERS-2, Sentinel-3 and ICESat-2.

2.1.2 Sea Ice Concentration

For sea ice concentration, we use the Ocean and Sea Ice Satellite Application Facility (OSI SAF) Global Sea Ice Concentration Climate Data Product (CDR) version 3 (OSI-450-a, 2022), which covers the period 1978 - 2020 and is routinely extended by the Interim CDR OSI-430-a. OSI-450-a is a full reprocessing of sea-ice concentration, using improved algorithms and an upgraded processing chain (Lavergne et al., 2023, 2019). Sea ice concentration is obtained from passive microwave radiometer data, including the scanning multichannel microwave radiometer (SMMR), the special sensor microwave/imager (SSM/I), and the special sensor microwave imager/sounder (SSMIS), as well as ERA5 reanalysis data. Ice concentration is provided on daily EASE2 grids with a spatial resolution of 25 km.

2.1.3 Sea Ice Drift

For sea ice drift, we use the OSI SAF low-resolution Global Sea Ice Drift CDR version 1 (OSI-455, 2022), which covers the period 1991 - 2020. OSI-455 provides displacements over a time span of 24 hours on a 75 km grid and is based on passive microwave radiometer data including satellite sensors SSM/I, SSMIS, the advanced microwave scanning radiometer for Earth Observing System (AMSR-E), and the advanced microwave scanning radiometer 2 (AMSR2). Displacements are estimated using a cross-correlation method on pairs of satellite images. OSI-455 builds on the methodologies of the near-real-time sea ice drift product OSI-405 (OSI-405, 2007). More details about the used algorithm can be found in Lavergne and Down (2023). If data on individual days are missing, the data product of the closest day available is used. OSI-455 also provides uncertainty estimates (one standard deviation) for the dX and dY components of the drift vector, which are used for the DA-SIT uncertainty estimation.

2.2 Drift-Aware Sea Ice Thickness Trajectories

Fig. 1 shows the processing scheme for the drift-aware sea-ice thickness (DA-SIT) product. The processing is divided into several steps, which are executed sequentially for each winter season. In the following we describe the individual steps required to compute DA-SIT, corresponding to Fig. 1.

2.2.1 Sea Ice Parcel Registration

In the first step, the along track SIT data products (Envisat, CryoSat-2) are collected on a daily basis. For the sea-ice parcel registration, these individual data points are aggregated within circular parcels with a radius of $R = \sqrt{2} \cdot 10\,\mathrm{km}$. This registration

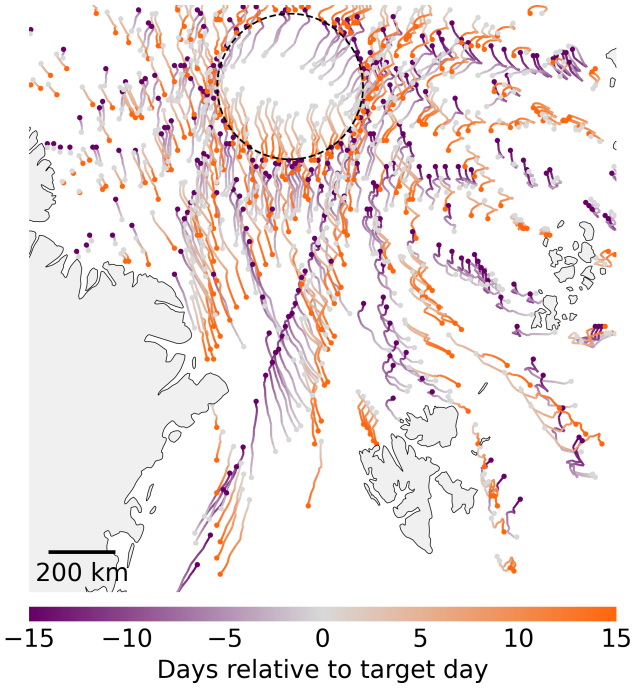

Figure 2. Every 10th sea ice parcel trajectory with origin in beginning or end of March 2020, and target day on the 15th of March. The black dashed circle at 88°N marks the CryoSat-2 pole hole.

in parcels is done to reduce computational costs of the drift correction step. The parcel-wise tracking is also justified considering the coarse spatial resolution of the drift product (see Section 2.1.3).

Location of parcel centres is selected using the NSIDC EASE-Grid 2.0 (Brodzik et al., 2012) with a spacing of 10 km in both x and y directions. The chosen radius ensures partial overlap between parcels, improving the robustness of SIT distribution representation and mitigating geolocation errors.

Parcels are initially registered using the centroid of each grid cell, corresponding to the central position of each circular polygon. The mean SIT is calculated for each parcel. To ensure the presence of sea ice, the OSI-450-a sea-ice concentration product is interpolated onto the initial parcel positions. Parcels with sea-ice concentrations below 15% are excluded from following processing steps.

2.2.2 Drift Correction

The drift correction is applied to parcels both forward and backward in time on a daily basis. The day onto which parcels are projected by applying the drift correction, is called *target day*. The OSI-455 displacements are first resampled onto the sea-ice concentration grid and then interpolated on parcel positions with a minimum sea-ice concentration of 15% using a bi-linear interpolation scheme.

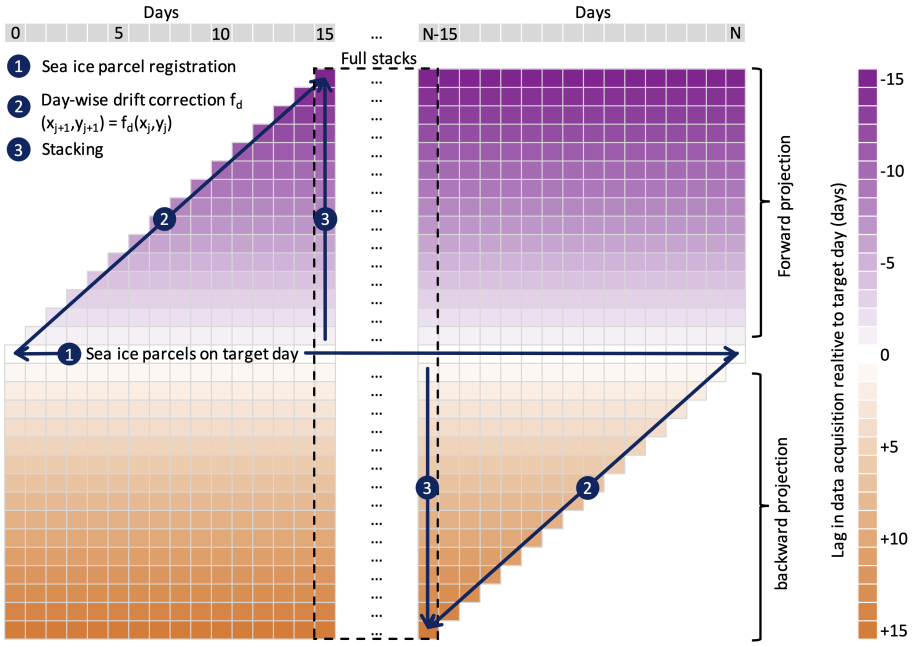

Figure 3. Processing scheme to produce the DA-SIT product. Each cell represents sea-ice observations of one day. The color map and vertical axis represent the delay regarding the time of data acquisition. Horizontal axis represents the ordinary timeline in day, e.g., day 0 may represent 1 October, and day N refers to 30 April. Diagonal aligned boxes (lower left to upper right for forward projection) represent daily trajectories, which are daily drift-corrected, containing the same SIT data from the day of acquisition.

The time bounds of the OSI-455 drift product span from 12:00 UTC on the previous day to 12:00 UTC on the day corresponding to the dataset registration time. The latter (12:00 UTC of the registration day) also serves as the reference time for the daily DA-SIT. Consequently, to correct drift on a given day, we use the drift product associated with a reference time set one day in advance.

For the initial drift correction of parcels, we first calculate the time difference between the registration time of the sea-ice parcel on the target day and the reference time of the drift product (12:00 UTC one day ahead). This difference is typically close to 24 hours. Using this time difference, we adjust the position of the sea-ice parcel accordingly. Following this correction, the reference time for all parcels is standardized to 12:00 UTC of the respective day. Subsequent drift corrections involve a consistent 24-hour displacement. We use a first-order Runge-Kutta integration scheme, equivalent to Euler's method. While a fourth-order scheme generally offers higher accuracy, it comes with significantly greater computational cost. Given that the drift vectors are defined on a 75 km grid and daily displacements are significantly smaller than this resolution, a higher-order scheme was not implemented.

Next, we use the OSI-450-a ice concentration corresponding to the day when the parcel reaches its updated position. Ice concentration is interpolated onto these updated positions, and any parcels located in areas with ice concentration below a threshold of 15% are removed, as we assume that ice drifting into open ocean will melt even during polar winter. Therefore,

those parcels are removed from the dataset. We also ensure that parcels do not unintentionally drift onto land grid cells, which can occasionally occur due to the low resolution of the drift product and related uncertainties.

As a result of the systematic drift correction, the original along-track SIT pattern disperses, transforming into a point cloud where each point represents a circular parcel. This process is repeated daily, progressively updating the positions of the parcels over time. This dispersion is illustrated in Fig. 2. The map shows a selection of parcel trajectories with a length of 15 days. The parcels originate either 15 days prior to or 15 days after the target day. While the parcels initially align with the satellite's track pattern, after 15 days they can drift by over 200 km in some cases.

2.2.3 Stacking Process

The stacking scheme is illustrated in Fig. 3. Processing typically begins on 1 October (Day 0), the first day after the summer pausing when altimetry processing resumes. On this day, sea-ice parcels are initially registered following the procedure described in Section 2.2.1. The drift correction, as outlined in Section 2.2.2, is then applied to these parcels. Each elapsing day, newly registered parcels, or parcels already corrected for drift on previous days, are advected. For each parcel, a maximum of 15 daily drift corrections is allowed. Parcels are removed from the stack after the 15th correction.

This procedure is performed in both forward and backward time directions. Each day, drift-corrected parcels are stacked onto the drift-corrected parcels from one day prior or one day ahead, depending on the direction. A set of parcels is organized in a data frame structure, which contains the parcel geometries and their trajectories from the initial registration until the end of the drift (nominally 15 days).

The trajectory of each parcel is represented as a list of points, beginning with its initial registration position and ending at its final drift-corrected destination. Forward-projected parcels have trajectories progressing forward in time, while backward-projected parcels have trajectories moving backward in time.

As shown in Fig. 3, starting with a set of parcels on Day 0, the process produces a stack of 31 parcel sets by Day 15. This includes 15 sets from forward projections, 15 from backward projections, and the initial parcel set derived from the along-track SIT product on the target day. The diagonals in Fig. 3 represent the same parcels (and therefore the same SIT data) but at varying positions within the space-time domain due to daily forward or backward drift corrections. Ultimately, the vertically stacked parcel sets, spanning both past and future days, represent the predicted parcel positions on the target day.

After completing the forward and backward stacking, the parcel sets within a single stack are merged to create the drift-corrected dataset for a given target day (Fig. 3). Specifically, the parcel sets are combined into a unified data frame. Since both the forward and backward stacks include the parcel set corresponding to the target day, one of these is removed to prevent duplication.

2.2.4 Growth estimation and correction

Growth estimation aims to correct the SIT of parcels for processes that alter the thickness along their space-time trajectory. While parcels are drift-corrected, their SIT remains fixed at the state of initial registration. However, dynamic and thermodynamic processes alter the thickness between the registration time and the target day, which is typically up to 15 days. To

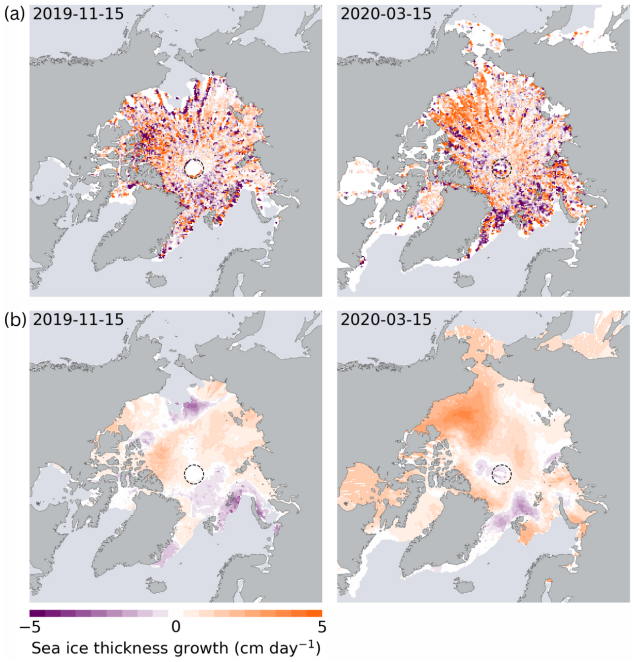

Figure 4. (a) Sea ice growth estimates from CryoSat-2 across the Arctic for November 2019 and March 2020 within a full stack of parcel sets covering one month. (b) Spatially interpolated sea ice growth based on growth estimates shown in (a). The white area in the background indicates data gaps with respect to the actual ice extent. The dashed circle represents the pole hole of the CryoSat-2 orbit coverage.

account for these changes, we make use of the drift-corrected ice parcels. The drift-correction ensures that parcels, which are collocated in space, but with different registration times, represent a snapshot of the same ice regime, observed at different times. This allows us to apply a linear growth model.

In the initial step of the growth correction process, we create a 25 × 25 km EASE2 grid. Next, we assign all parcels from the full stack to their corresponding grid cells. When a grid cell contains at least three parcels with SIT estimates from different points in time, we apply a least-squares linear fit:

$$f_H(n) = p_1 n + p_0 \tag{1}$$

where f_H is the fitted sea ice thickness, and n representing the number of days between the day of measurements and the target day. p_0 is the projected SIT on the target day. The coefficient p_1 represents the SIT growth, which can be positive or negative. It is important to note that, at this stage, we do not differentiate between thermodynamic and dynamic growth processes. Additionally, we acknowledge that due to uncertainties in the drift product and nonuniform altimeter measurement coverage within parcels, exact spatial collocations are unlikely. Nonetheless, we assume SIT values are representative within a given area, chosen here as 25 × 25 km, which is smaller than typical SIT correlation lengths in the Arctic (Ricker et al., 2017). Therefore, this method is representative of average ice thickness at grid resolution scale, neglecting thickness variations between individual sea ice floes. The linear fitting generates a covariance matrix, which quantifies the uncertainty of p_1. This uncertainty is later

used for the overall uncertainty estimation. Fig. 4a illustrates an example of gridded growth estimates derived from a stack of trajectories centered on 15 November 2019 and 15 March 2020. These estimates represent ice growth over one-month periods. The density of growth estimates across the Arctic decreases with latitude as the orbit density decreases. Therefore, uncertainties of these estimates increase with distance from the pole. In some regions, very high and very low growth rates appear side by side, and overall, the gridded growth estimates exhibit considerable noise. This is partly because the linear fit is highly sensitive to abrupt changes in SIT, which may occur naturally or result from measurement uncertainties. Such variability can introduce significant noise or bias into the estimated growth rates. Additionally, the SIT estimates used for the fit are obtained over differing time intervals, leading to inconsistencies in temporal resolution. These inconsistencies can degrade the stability of the fitted growth estimates.

To achieve a consistent growth correction, we fill the gaps that are left where not enough collocated parcels from different times could be identified. Here we use a radial basis function (RBF) interpolation in two dimensions with a Gaussian kernel based on the scipy.interpolate.RBFInterpolator function (Virtanen et al., 2020). An RBF interpolant based on data values d at locations y is a linear combination of RBFs centered at y, and a polynomial $P(x)$ of a specific degree, evaluated at position x (Virtanen et al., 2020):

$$f(x) = K(x,y)a + P(x)b \tag{2}$$

where $K(x,y)$ is an array of RBFs centered at y and evaluated at x. The coefficients a and b solve the linear equations:

$$\left(K(y,y) + \lambda(\Phi)I\right)a + P(y)b = d \tag{3}$$

$$P(y)^T a = 0 \tag{4}$$

Here, $\lambda(\Phi)$ is a smoothing scale parameter, chosen to be latitude-dependent to account for the varying density of measurement points caused by the satellite's orbital geometry. The smoothing scale parameter decreases linearly from 80 at $\Phi = 40°\mathrm{N}$ to 10 at $\Phi = 90°\mathrm{N}$. For further details on the RBF interpolation method, we refer to Virtanen et al. (2020).

To minimize computation time, we limit the number of nearest data points used for each interpolation to a maximum of 260. Fig. 4b illustrates an example of spatially interpolated sea ice growth for 15 November 2019 and 15 March 2020, corresponding to Fig. 4a. The interpolated ice growth values are then applied to adjust the SIT estimates of the parcels, considering the number of days between the actual measurement date and the target day. Finally, parcel trajectories aggregated over one month are exported in daily comma-separated value (csv) files (Fig. 3).

2.2.5 Computing performance

The computing efficiency of the stacking process benefits from parallel processing, which is implemented in the DriftAware-SIAlt Python software. On a high performance computing cluster (HPC), using 16 cpu cores and 8 GB memory per cpu, processing of csv files with DA trajectories for an entire winter season (October-April) takes approximately 4 hours. A set of daily csv files containing the DA trajectories for one winter season requires approximately 30 GB, with individual file sizes between 40 and 170 MB.

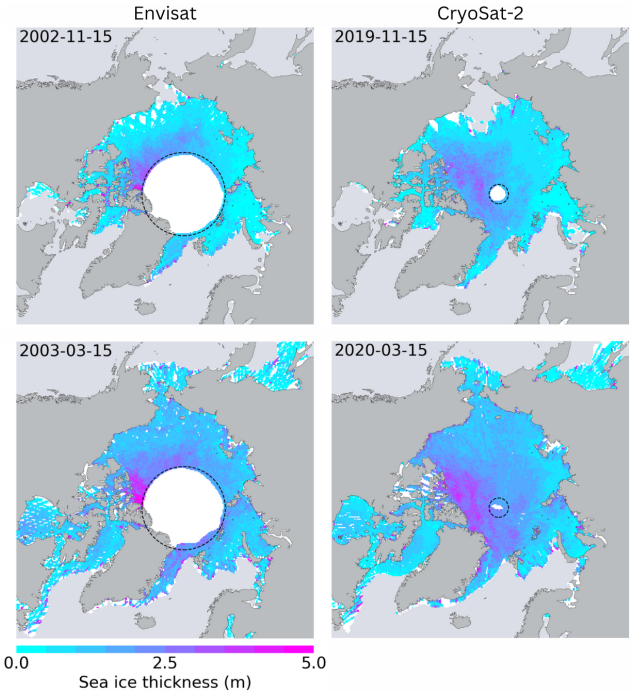

Figure 5. Drift-aware sea-ice thickness from Envisat (2002/2003) and CryoSat-2 (2019/2020) for November and March with applied sea ice growth correction. The white area in the background indicates data gaps with respect to the actual ice extent. The dashed circle represents the pole hole of the Envisat/CryoSat-2 orbit coverage.

2.3 Evaluation on the EASE2 grid

We evaluate the stacked, now SIT growth-corrected, parcel sets on a 25 km EASE2 grid, in line with other existing SIT products (e.g., Ricker et al. (2017)) and the SIC climate data record. We average SIT of the parcel sets at their positions at the respective target day within 25 km grid cells. This means we will retrieve daily DA-SIT grids, each containing data from a monthly window (15 days in both directions). Therefore, to provide gridded products that contain entirely independent data, we must consider the daily stacks with 1 month difference in reference time. To align with the conventional monthly gridded products, we select the mid-month stacks to compute the respective DA-SIT grids, i.e., on the 15th of each month. During the ramping phase in the beginning and end of the processing period, stacks are not full, and therefore gridded maps will be incomplete within the first and last 15 days of the processing period (Fig. 3).

The average SIT (H_{L3}) for one grid cell is computed as an arithmetic mean, ignoring non-numeric values:

$$H_{L3} = \frac{1}{n_{L2}} \cdot \sum_{i=0}^{n_{L2}} H_{i,L2} \quad \text{if } H_{i,L2} \neq \text{NaN} \tag{5}$$

where n_{L2} is the number of parcels inside the corresponding grid cell.

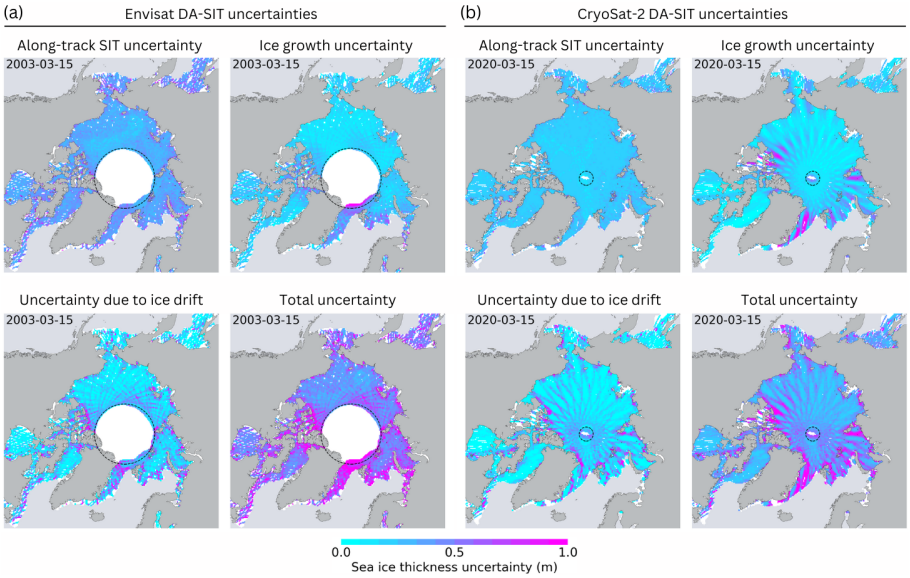

Figure 6. a) Uncertainty components of Envisat DA-SIT product for 15 March 2003. b) Uncertainty components of CryoSat-2 DA-SIT product for 15 March 2020. The white area in the background indicates data gaps with respect to the actual ice extent. The dashed circle represents the actual pole hole of the Envisat/CryoSat-2 orbit coverage.

Fig. 5 shows the final gridded DA-SIT for Envisat (November 2002 and March 2003) and CryoSat-2 (November 2019 and March 2020) after SIT growth correction. The drift-correction can cause parcels sliding into the pole hole, reducing its size. But the drift-awareness can also result in data gaps like in the Chukchi Sea in November 2002. Those gaps arise when the satellite's orbital drift aligns in both direction and magnitude with the drift of the sea ice. In fact, this means that DA-SIT also reveals sea ice areas that have never been surveyed by the satellite within the one-month observation period.

2.4 Uncertainties

We distinguish between three major contributors to uncertainties of the gridded DA-SIT:

1. The uncertainty associated with the along-track SIT retrieval, used as input for drift-aware processing, is derived from the Level-2 along-track SIT of the CCI climate data record version 3.0 .

   The uncertainty of the mean SIT ($\sigma_{H_{parcel}}$) for each parcel is computed by considering the individual uncertainties of measurements associated to the parcel:

$$\sigma_{H_{parcel}} = \frac{\sqrt{\sum_{i=1}^{n} \sigma_i^2}}{n} \tag{6}$$

   where σ_i represents the uncertainty associated with the i-th measurement, and n is the total number of measurements. This calculation assumes that the uncertainties are uncorrelated.

2. The uncertainty of SIT as a consequence of the drift uncertainty depends on two factors. First, the uncertainty of the ice drift product, and second, the spatial variability of SIT in the area where the parcel might have been drifted into, considering the drift uncertainty. We start with aggregating the drift uncertainty along the parcel trajectory. In OSI-455, the daily drift uncertainty estimates, σ_{D}, are identical in both the x and y directions. For each step of drift correction, the squares of the drift uncertainties are aggregated. After the final drift correction, the drift uncertainty, $\sigma_{D_{x,y}}(t_j)$, of a parcel at the target day t_j is computed as follows:

$$\sigma_{D_{x,y}}(t_j) = \sqrt{\sum_{i=j-N}^{j} \left(\sigma_{D_{x,y}}(t_i)\right)^2} \tag{7}$$

where N is the number of days over which drift correction is performed (up to 15 days), t_j represents the time of the target day assigned the index j, and i represents the day of data acquisition (the starting point of the drift). In the second step, we analyze the impact of the spatial SIT variability. After the merging of forward and backward stacks including growth correction (Sections 2.2.3 and 2.2.4), all neighboring ice parcels within the area defined by the drift uncertainty are aggregated at each parcel's final position.. The aggregation uses a radius defined as $\sqrt{2}\sigma_{D_{x,y}}(t_j)$, where $\sigma_{D_{x,y}}(t_j)$ represents the estimated uncertainty in the x and y directions.

This results in a SIT distribution over the area where the ice parcel may have drifted, accounting for the drift uncertainty. If the thickness in this area is highly homogeneous, significant uncertainties in SIT are not expected, as the varying position of the ice parcel will not alter the SIT distribution within the area. Conversely, if the SIT in this area is highly heterogeneous, with substantial gradients, a different position of the ice parcel could result in changes to the SIT at its location. To estimate the potential uncertainty in SIT within the drift uncertainty radius, we calculate the inter-quartile range of the SIT distribution in that area, defined as the difference between the 75th and 25th percentiles. However, if the drift uncertainty radius does not exceed the radius of the parcel area, the resulting SIT uncertainty is set to 0. This is especially the case for fastened sea ice.

3. The uncertainty due to SIT growth and its correction is estimated from the covariance matrix obtained through linear fitting, which is used to estimate SIT growth (Section 3.6). For each parcel's growth estimate, the growth uncertainty, σ_{H_G}, is computed as follows:

$$\sigma_{H_G}(\Delta t) = \sqrt{\sigma_{p_1}^2}\Delta t \tag{8}$$

where $\sigma_{p_1}^2$ is the variance term of the growth coefficient p_1, derived from the diagonal elements of the covariance matrix. p_1 is multiplied by the time difference Δt, measured in days, between the target day and the day of data acquisition to calculate the SIT uncertainty due to ice growth for a given ice parcel.

The total uncertainty is calculated by the square root of the sum of the squares of the three individual components. Fig. 6 shows the three uncertainty components as well as the total uncertainty of DA-SIT for Envisat (15 March 2003) and CryoSat-2 (15 March 2020). The along-track SIT uncertainty is relatively uniform across the Central Arctic, but larger along the coastlines

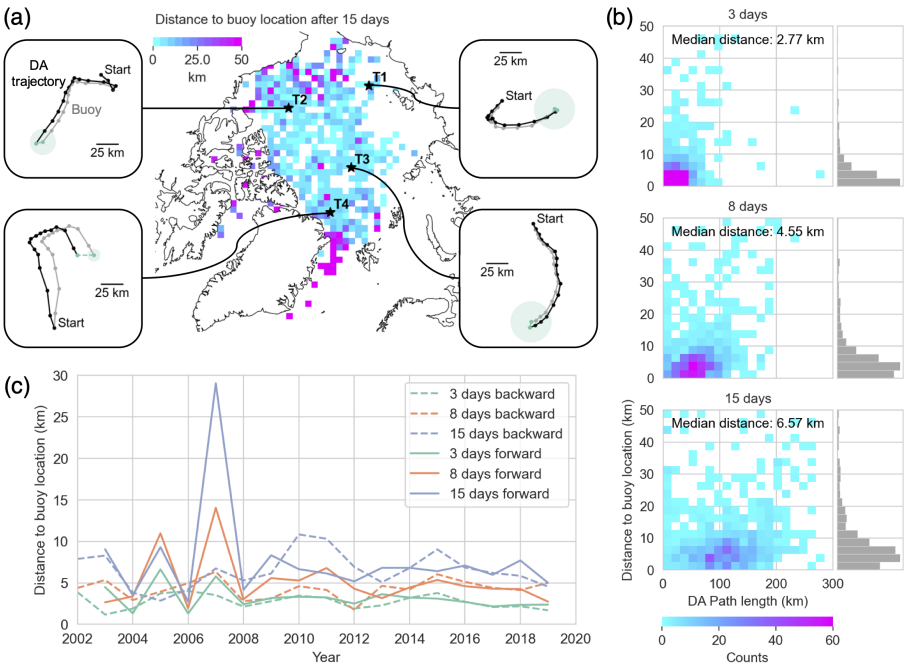

Figure 7. (a) Validation of DA trajectories with buoys, including example trajectories (T1-4). Green-filled circles represent the DA-uncertainty of the drift correction after ±15 days. (b) Distance between DA-SIT and buoy trajectory after 3, 8 and 15 days, as a function of DA path length. (c) Yearly mean distance between DA and buoy trajectory after 3, 8 and 15 days in both directions.

and over thinner ice Ricker et al. (2017). Moreover, the pulse-limited RA-2/Envisat radar measurements generally cause higher along-track sea ice thickness (SIT) uncertainty compared to CryoSat-2. The SIT uncertainty caused by ice drift is significantly smaller in the pack ice but becomes more pronounced in the marginal ice zone and especially along coastlines. This is primarily due to the greater uncertainty in drift products near coastlines, whereas the relatively low drift uncertainties in the pack ice zone often result in accumulated displacement uncertainties that remain smaller than the radius of the sea ice parcel cell. It is also worth noting that examples from recent years benefit from the AMSR2 mission, starting in 2012. Earlier years, dominated by the SSM/I missions, may exhibit larger drift-related uncertainties. More information on the ice drift uncertainties are provided in Lavergne and Down (2023) and Sumata et al. (2014). The SIT uncertainty due to ice growth shows a distinct orbital pattern, a result of the growth uncertainty being a function of the elapsed time between data acquisition and target day. The total uncertainty pattern is, therefore, a superposition of the patterns of the individual components.

3 Validation of the Drift-Aware Sea Ice Thickness

3.1 Validation of DA-SIT Trajectories using Buoys

We use trajectories from autonomous buoys to validate the DA-SIT trajectories. We use buoy data provided by the International Arctic Buoy Program (IABP). The IABP includes different types of buoys that measure snow and ice parameters such as ice temperature, snow depth, and SIT. However, for this study, we only use the buoy positions. Although IABP also includes ice mass balance buoys to measure sea ice thickness, we do not use them for the SIT evaluation, as their measurements only represent the sea ice at their immediate position, and are therefore not suited for comparing with satellite observations, which require the integration of SIT measurements over at least several hundred meters. In total we use 1029 buoys. The original sampling frequency of the buoy data was 3-hourly until 2016 and hourly thereafter. We resample the IABP buoy data to daily positions at 12:00 UTC to align with the reference time of the DA-SIT trajectories. The daily buoy positions are then divided into 31-day periods, centered on a target day with a $\pm$15-day window to align with the DA-SIT trajectories. For the starting dates of the 15-days buoy trajectories, we identify the spatially closest initial DA-SIT ice parcels from all available trajectories. This includes both trajectories in forward and backward direction. We set a maximum distance threshold of 25 km between the buoy and the initial DA-SIT ice parcel position. This threshold is well below the spatial resolution of the drift product, minimizing any significant impact of positional offsets between the initial positions of the parcel and the buoys.

Fig. 7a shows a map of distances between the end points of individual DA-SIT trajectories, and the corresponding buoy trajectories. We consider only the distances after 15 days of drift, either backward or forward in time. The pattern indicates higher uncertainties of the DA-SIT trajectories in the Fram Strait and East Greenland Sea as well as in the marginal ice zones and in peripheral locations. Here the discrepancy after 15 days of drift correction can reach more than 50 km. In contrast, the Central Arctic shows distances of typically less than 10 km, which is below grid-cell size.

Fig. 7b shows the linkage between the uncertainty of the DA-SIT trajectory and path length. The path length is the covered distance along the trajectory. It begins on the day of the measurements and ends on the target day and is generally increasing with time. With increasing time lag and path length, also the distance between buoy location and DA ice parcel location is increasing. While after 3 days, we observe a median distance of 2.77 km considering all co-registered trajectories, it increases to 6.57 km after 15 days. Therefore, we conclude that with increasing DA time lag, the uncertainty in the respective ice parcel location increases. This uncertainty is described in section 2.4 and displayed in the four trajectory examples in Fig. 7a. Fig. 7c shows the yearly mean distance between DA-SIT parcel and buoy location for all co-registered trajectories across the Arctic, after 3, 8, and 15 days. There is no significant trend in the distances between buoy and DA ice parcel within the 2002-2020 period. We also do not observe a significant difference in the distances between backward and forward projected trajectories. However, as discussed before (Fig. 7b), we observe a dependency of the distance on the time lag. The longer the time lag between target day and day of measurements, the higher the discrepancy between buoy and DA-SIT parcel location.

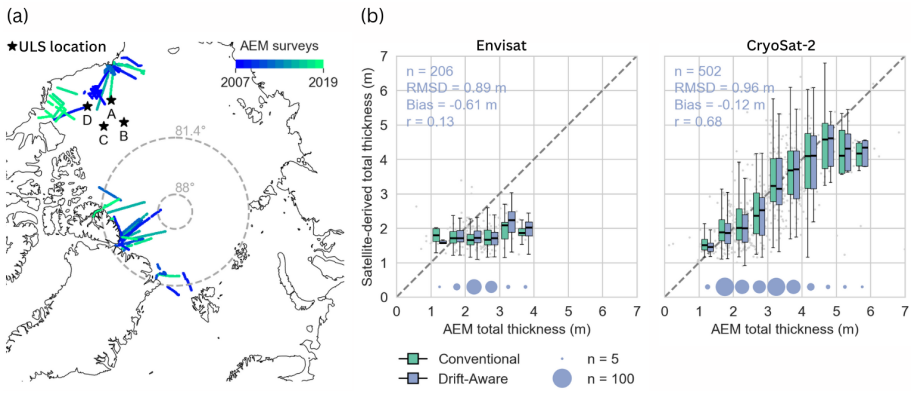

Figure 8. (a) Overview of DA-SIT validation data across the Arctic. Airborne electromagnetic thickness sounding (AEM) surveys are sorted by year. The black stars indicate the locations of the ULS (BGEP moorings). (b) Box-and-whisker plots of total DA-SIT and conventionally gridded SIT (separated between the Envisat and CryoSat-2 eras) plotted against binned AEM total sea ice thickness. Grey dots in the background represent the actual distribution. The scaled circles below the Box-and-whisker plots indicate the number of points for each bin. The bin width is 0.5 m.

3.2 Validation with Airborne EM

Airborne electromagnetic induction thickness sounding (AEM) is a method to measure total sea ice thickness directly. The EM-Bird is an AEM sensor that is towed over sea ice by a helicopter or fixed-wing aircraft (Pfaffling et al., 2007; Haas et al., 2009). The distance to the sea ice/seawater interface is calculated from the EM response. The sea ice + snow/air interface is obtained from a laser altimeter. The difference between the two interfaces corresponds to the sea-ice + snow thickness. The point spacing of the measurements is approximately 5 m.

We use AEM data from helicopter and fixed-wing aircraft campaigns during the period 2007-2019 (Table A1). AEM data are projected and averaged on a 25 km EASE2 grid, in line with the gridded DA-SIT. Since the AEM data represent total thickness, which combines SIT and snow depth, we need to convert the DA-SIT estimates accordingly. In the drift-aware processing, the snow depth from the along-track data is assigned to parcels in the same way as SIT, and is therefore also drift-corrected. Consequently, we add the gridded snow depth to the DA-SIT retrieval to obtain DA total thickness. Daily grids of AEM data are then compared with the matching DA-SIT grids. The validation of the gridded DA-SIT product against total ice thickness is carried out for both the Envisat and the CryoSat-2 era and allows to evaluate the spatial distribution of SIT at a given time. Due to the larger Envisat pole hole (>81.4°N), suitable AEM surveys are primarily limited to the Beaufort and Chukchi Sea (Fig. 8a). Therefore, the surveyed ice does not contain as thick and deformed ice as in the Lincoln Sea for example. The CryoSat-2 orbit domain extends up to 88°N and thus also includes AEM surveys over thick, deformed multiyear sea ice. Fig. 8b shows validation results for each satellite era. The bias is -0.61 m for Envisat and -0.13 m for CryoSat-2. The root mean square deviation (RMSD) is comparable between the two sensors, measuring 0.89 m for Envisat and 0.98 m for CryoSat-2. The Pearson correlation differs significantly, with a value of r=0.68 for CryoSat-2 and only r=0.13 for Envisat. The weak

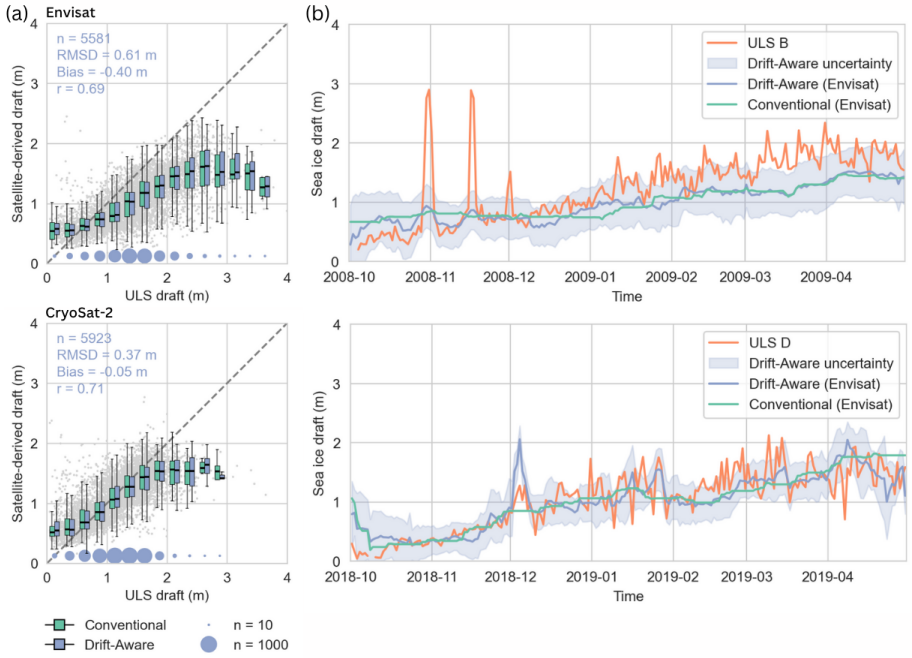

Figure 9. (a) Box-and-whisker plots of daily DA-draft and conventionally gridded ice draft (Envisat 2002–2012, CryoSat-2 2010–2020) plotted against binned daily averaged ULS draft. Grey dots in the background represent the actual distribution. The scaled circles below the Box-and-whisker plots indicate the number of points for each bin. The bin width is 0.25 m (b) Daily sea ice draft from ULS and the co-registered DA-draft as well as ice draft from conventionally gridded SIT over the winter seasons 2008/2009 (CryoSat-2) and 2018/2019 (CryoSat-2).

correlation and slight underestimation of thickness observed in the Envisat data can be attributed to the limitations of its pulse-limited altimeter type, which lacks the capability to adequately capture deformed sea ice (Paul et al., 2018). For reference, Fig. 8b also shows the total sea ice thickness derived from conventional gridding (C-SIT), which does not include drift-awareness, but using the same gridding scheme (Section 2.3). For C-SIT, parcel positions are taken at the time of the satellite overflight and are gridded by aggregating data within a daily-shifting one-month time window. The comparison between DA-SIT and C-SIT with regard to the validation with AEM reveals only minor differences. This suggests that the effect of drift-awareness is mostly over-ruled by other sources of uncertainty like the limitations due to the satellite footprint in contrast to the high-resolution airborne measurements. The direct comparison between DA-SIT and C-SIT is discussed in Section 4 in more detail.

3.3 Validation with ULS

Upward looking sonars (ULS) are mounted on oceanographic moorings (Hansen et al., 2013; Krishfield et al., 2014) and provide information on long-term ice thickness variability and seasonal changes. ULS are used to derive ice draft by measuring the travel time of a sonar pulse transmitted by the ULS and reflected back from the ice bottom. The ice draft can then be

converted into ice thickness assuming snow load and densities of snow and ice. In contrast to AEM, ULS are valuable to evaluate the temporal change in sea ice draft in the vicinity of the ULS location. We use ULS ice draft data from moorings that have been deployed at four different sites in the Beaufort Sea within the Beaufort Gyre Exploration Project (BGEP, Krishfield et al. (2014)). Fig. 8a shows the position of the moorings in the Beaufort Sea. Their draft time series cover the Envisat (A, B, C, D), as well as the CryoSat-2 era (A, B, D). Exact locations and data record periods for the ULS A-D are provied in Table A2.

The original data are sampled at 2s intervals. We first remove open water sections. Afterwards, the filtered data were averaged over 24 h to obtain daily mean effective ice thickness for each ULS. Then, for each day and each ULS position, we co-register the nearest three grid cells in the DA-SIT grids. The thicknesses and uncertainties of the three grid cells are averaged. As the ULS provide draft estimates, we convert the co-registered DA-SIT into ice draft using climatological densities for ice ($900\,\mathrm{kg\,m^{-3}}$), snow ($300\,\mathrm{kg\,m^{-3}}$), and water ($1025\,\mathrm{kg\,m^{-3}}$). The snow depth is obtained from the DA-SIT product, which contains snow depth inherited from the L2P along track data.

Fig. 9 shows results from the comparison between the ULS and sea ice draft derived from DA-SIT (DA-draft). As for the comparison with AEM, the figure also includes ice draft derived from C-SIT as a reference. Fig. 9a shows the comparison between all BGEP ULS and DA-draft for the Envisat (2002-2012) and CryoSat-2 (2010-2020) eras. Combining all ULS, we find a bias of -0.4 (-0.05) m and a RMSD of 0.61 (0.37) m for the comparison with Envisat (CryoSat-2) DA-draft. Considering Envisat DA-draft, results suggest that SIT is generally underestimated, agreeing with the results from the AEM comparison. Again, this is also in agreement with the findings of the validation of the CCI SIT CDR. Khvorostovsky et al. (2020) provide a detailed comparison between BGEP ULS data and the CCI SIT CDR. They conclude that the sea ice draft growth underestimation observed for the most of winter seasons depends on the surface properties preconditioned by the melt intensity during the preceding summer. In our study, this is particularly true for Envisat, while CryoSat-2 DA-draft shows a better agreement with regard to the RMSD and Bias. This is expected because of the smaller footprint of CryoSat-2, and therefore higher sensitivity for deformed, thick ice. The discrepancy for draft classes > 2m for CryoSat-2 DA-draft may be due to the small sample size (< 15) per ULS draft bin. Unlike the AEM comparison, the Pearson correlation between DA-draft and ULS draft is similar for CryoSat-2 (r = 0.71) and Envisat (r = 0.69). This is partly because the ULS locations remain largely consistent across both satellite periods, sampling similar ice types. The evaluation of sea ice draft derived from C-SIT yields very similar results, consistent with the findings from the AEM comparison.

While the Box and Whisker plots for all ULS in Fig. 9a provide a general assessment, they do not capture the actual co-variability between datasets. To address this, we also evaluate the seasonal evolution of co-variability between the daily ice draft measured by the ULS and the co-registered DA-derived draft. Fig. 9b shows two winter seasons: 2008/2009 with ULS B ice draft compared to Envisat DA-draft, and 2018/2019 with ULS D ice draft compared to CryoSat-2 DA-draft.

The DA-draft captures the overall thermodynamic growth signal throughout the winter. In contrast, the short-term variability observed in the ULS data arises from changes in the ice draft as ice floes of different types and thickness drift through the sonar beam. This variability is driven by sea ice dynamics, where thicker, deformed ice and ridges formed during convergence coexist with thinner, newly formed ice resulting from divergence. The drift-awareness algorithm provides colocation on a

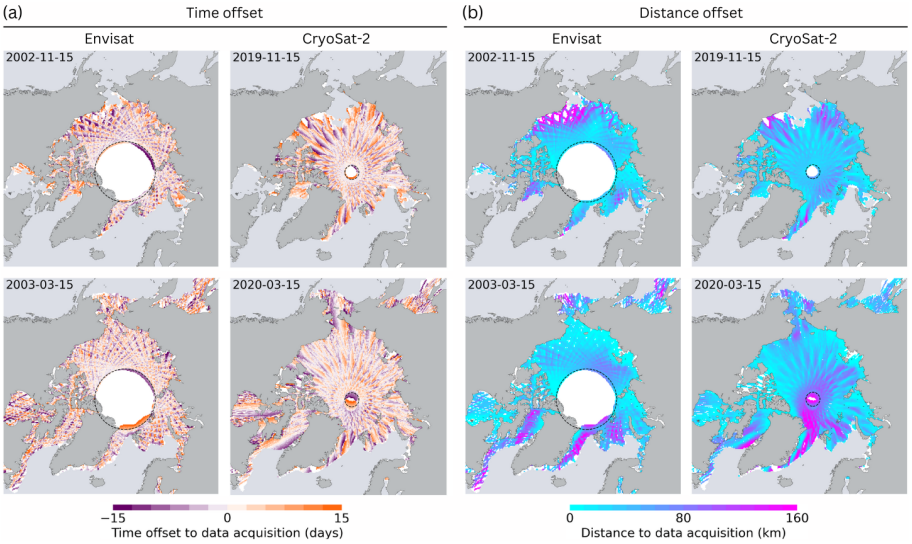

Figure 10. (a) Gridded time difference between the target day and the data acquisition time for Envisat (2002/2003) and CryoSat-2 (2019/2020), for 15 November and 15 March. (b) Same as (a) but for the geodesic distance between parcel position on the target day and at the time of the data acquisition. The white area in the background indicates data gaps with respect to the actual ice extent. The dashed circle represents the pole hole of the Envisat/CryoSat-2 orbit coverage.

spatial scale of a few kilometers, as discussed in Section 3.1. Moreover, the DA-draft is affected by uncertainties originating from the processing of the altimetry raw data (Ricker et al., 2014). Consequently, the ice draft measured by the ULS and the co-registered DA-draft often do not align precisely. As a result, we presume that the variability in DA and ULS draft is frequently out of phase.

However, some periods are in good agreement between the two datasets. For instance, in autumn 2008 we observe two distinct anomalies in the ULS B draft that can be also observed in the DA-draft (Envisat), although weaker. Similar, at the beginning of December 2018, both ULS D and DA-draft (CryoSat-2) reveal a sharp increase in ice draft, likely caused by a cluster of very thick ice drifting over the ULS. We believe that due to the limited resolution of the drift product and the differences in the illuminated areas between satellites and ULS, even after applying the DA algorithm, daily SIT averages of ULS and parcel thickness will be out of phase. But Fig. 9b indicates that, in some cases, the DA-algorithm captures SIT anomalies observed by the ULS, unlike the flat draft profile derived from C-SIT.

4 Impact Analysis

4.1 Time and Distance Offset to Data Acquisition

For each parcel, we track the time offset between the start and end of each parcel trajectory. The maximum offset is given by the time widow, that defines over how many days along track data are drift-corrected and stacked. In this study, we use $\pm$

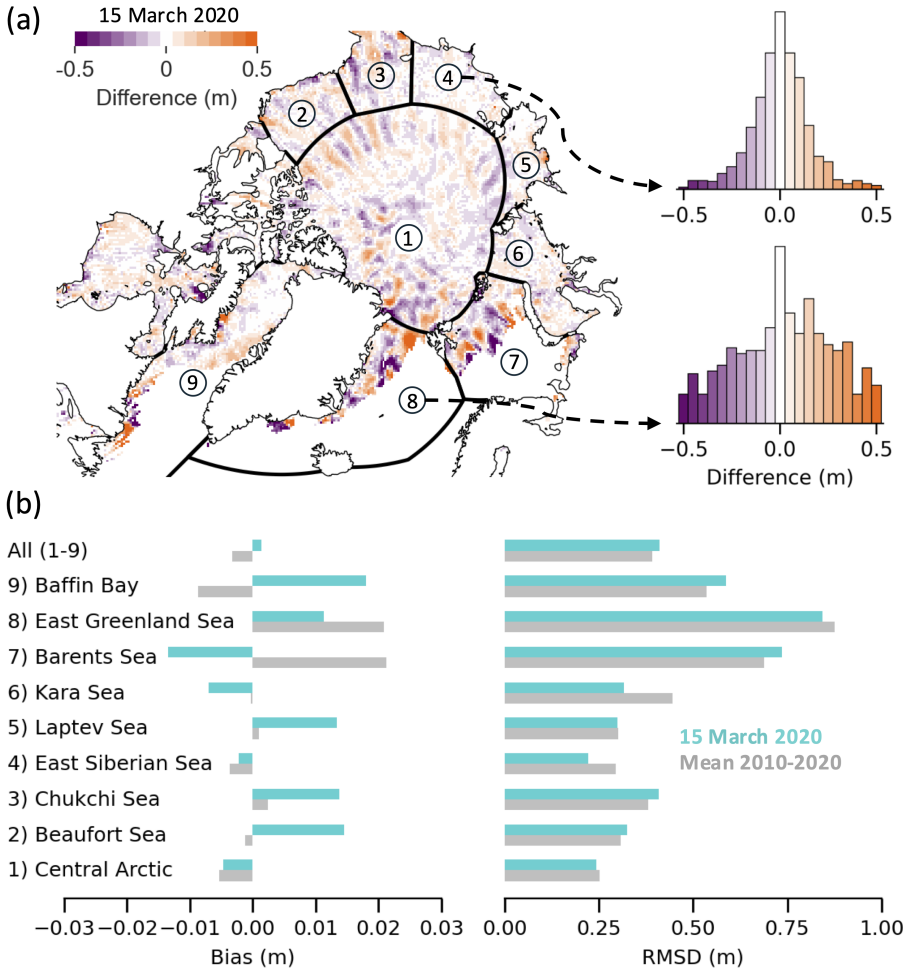

Figure 11. Intercomparison between DA-SIT and conventionally gridded SIT (C-SIT). (a) Difference map for 15 March 2020, including histograms of differences for the East Siberian Sea and East Greenland Sea. (b) Bias and root mean square deviation (RMSD) for marine regions on 15 March 2020, as well as the mean values over the 2010–2020 period.

15 days to be in line with the satellites sub cycle. Fig. 10a shows the gridded time offset for Envisat and CryoSat-2 DA-SIT parcels respectively, considering the beginning (November) and end (April) of the winter season. Due to the drifting satellite orbit, we observe a track pattern, with alternating time offsets in meridional direction. The thickness change along the parcel trajectory correlates with the time offset, because of thermodynamic ice growth as well as the accumulation of deformation. As a consequence, neglecting ice drift and ice growth corrections, the time offset pattern will cause track patterns in the monthly SIT maps.

Similar, we calculate the geodesic distance between the final parcel position after drift correction, and the position at the time of the measurements. Fig. 10b shows the gridded geodesic distance for the same sensors and months as in Fig. 10a. The

distance depends mainly on three factors. First, the travel distance scales with the temporal offset (Fig. 10a) for a given sea ice motion vector. Second, the magnitude of the sea ice drift, and third, its heading, affect how far the parcel has traveled from the location of the satellite overflight. For example, high, southerly directed ice drift in the Fram Strait leads to large distances to the location of data acquisition, scaled by the time offset. Those patterns are highly variable as they directly depend on the sea ice drift. In the Fram Strait in March 2020, we find distances of up to 200 km, which is equal to the width of 8 grid cells. This means, neglecting the ice drift correction in regions of high drift rates, will cause incorrect localization of thickness anomalies in heterogeneous sea ice regimes.

4.2 Comparison with conventional Sea Ice Thickness Grids

The key difference between the DA-SIT product and the baseline CCI SIT is the drift-awareness as DA-SIT is based on the same along-track retrievals. Therefore, we compare DA-SIT with the conventionally gridded C-SIT (Section 3.2). Here we only present the results from the CryoSat-2 era, as we find very similar results for the Envisat era. Fig. 11a shows the difference map between DA-SIT and C-SIT for 15 March 2020. We divide the Arctic into maritime regions, introduced by Meier and Stewart (2023). For these regions, we calculate the bias and RMSD between DA-SIT and C-SIT, shown in Figure 11b). The example from 15 March 2020 highlights regional differences in the magnitude of the impact of drift-awareness. In the East Greenland Sea, including Fram Strait, we generally find the highest RMSD, while the lowest RMSD for March 2020 is found in the East Siberian Sea. Considering the entire CryoSat-2 era (2010-2020), the Arctic Ocean exhibits the lowest RMSD. As displayed by the histograms of differences in Fig. 11a, the distributions can be close to Gaussian or Laplace shape (e.g. East Siberian Sea), but can also be slightly skewed (e.g., East Greenland Sea). Typically, the smaller the area considered, the larger the differences. The pattern of differences in Fig. 11a reveals that the strongest impact of drift-awareness is found in regions with strong sea ice drift, e.g., Fram Strait, Beaufort Gyre and Barents Sea. In the Beaufort Sea region and north of it, we observe an alternating pattern of positive and negative differences in meridional direction. This originates from the fact that the C-SIT does not take into account the drifting along track measurements, which contributes to the typical orbit track pattern (known as trackiness), which sometimes can be observed in the conventional SIT maps (Ricker et al., 2014). As expected, the DA-SIT product reduces this effect. The overall bias between DA-SIT and C-SIT is -0.33 cm for the period 2010–2020 across all considered regions, which means that the impact on mean Arctic SIT and volume time series is negligible.

5 Conclusions

We have presented a method to ensure drift-awareness (DA) for sea ice thickness (SIT) maps derived from satellite altimetry and demonstrated its application on Envisat and CryoSat-2 data within the framework of the ESA Climate Change Initiative. The study included method descriptions, validation, and impact analysis. By applying DA, SIT retrievals from one month of altimetry measurements are projected onto one day, allowing to produce daily maps of Pan-Arctic SIT. This approach facilitates comparisons with SIT derived from passive microwave radiometer measurements (Tian-Kunze et al., 2014) or in-situ observations. From our findings in this study, we draw the following conclusions:

1. **Validation with Observational Data:** The DA-SIT method can capture anomalies observed in daily upward-looking sonar (ULS) averages, depending on the spatial extent of the anomalies and accurate colocation of measurements. This highlights the method's capacity for improved regional analyses, though uncertainties in drift corrections must be considered.

2. **Improvement in spatial representation:** Drift-awareness improves the spatial representation of sea ice thickness in gridded products by reducing regional biases (10–20 cm) and minimizing displacement errors (up to 200 km) caused by neglecting sea ice drift. This improvement is particularly important in regions with strong drift, such as the Beaufort Sea and East Greenland Sea.

3. **Regional vs. Pan-Arctic Effects:** While regional-scale biases can be significant, the pan-Arctic mean differences between drift-aware SIT (DA-SIT) and conventional SIT maps are negligible (0.29 cm across all regions from 2010–2020, Fig. 11). This is because regional biases balance out on a larger scale, as ice is redistributed rather than lost.

4. **Applications across missions:** The DA algorithm is applicable to other satellite altimeters such as ERS-1/2, Sentinel-3A/B, and ICESat-2. Drift-awareness should be integrated into future SIT mapping efforts to reduce uncertainties, especially when merging data from different missions, for example radar (e.g., CryoSat-2) and laser altimeters (e.g., ICESat-2) to derive snow depth.

5. **Future satellite missions:** Drift-awareness will be particularly important for new advanced altimeters, such as the Copernicus Polar Ice and Snow Topography Altimeter (CRISTAL) (Kern et al., 2020). To fully leverage the high-resolution measurements these systems provide, DA should be combined with higher-resolution drift products, e.g., derived from synthetic aperture radar (SAR) data (Howell et al., 2022) or future radiometer observations like the Copernicus Imaging Microwave Radiometer (CIMR) (Lavergne et al., 2021).

Overall, incorporating drift-awareness in sea ice thickness mapping enhances the accuracy of gridded products, supports climate monitoring, and improves the understanding of sea ice dynamics. In future, we plan to apply the drift-awareness on altimetry retrievals in the Southern Ocean. Moreover, implementation of a column model that estimates dynamic and thermodynamic SIT growth along the DA trajectories could provide complementing information, which help to interpret the satellite-derived SIT estimates. Moreover, implementing near-real-time (NRT) processing using the most recent 15 days of altimetry data, combined with NRT sea ice drift, has the potential to improve NRT SIT distributions.

Code and data availability. All data that have been used or produced in this study are publicly available:

- The DA-SIT data record (v100) is available on Zenodo: https://doi.org/10.5281/zenodo.14733131, last access 24 Jan 2025.
- Sea ice drift (OSI-455) and concentration (OSI-450-a) were obtained from ftp://osisaf.met.no, last access 20 Jan 2025.
- Envisat and CryoSat-2 level-2 along track data, produced within the ESA CCI project, were obtained from the ftp server hosted by the Alfred Wegener Institute (ftp.awi.de/sea_ice/projects/cci/crdp/v3p0, last access: 20 Jan 2025).

- AEM data were obtained from the PANGAEA data portal (Felden et al., 2023) (https://www.pangaea.de, last access: 20 Jan 2025).
- BGEP ULS data were obtained from the Woods Hole Oceanographic Institution (https://www2.whoi.edu/site/beaufortgyre/data/, last access: 20 Jan 2025).
- Bouy data were obtained from the IABP (https://iabp.apl.washington.edu/data.html, last access: 20 Jan 2025):
  - 3-hourly data (until 2016) were obtained from https://iabp.apl.washington.edu/Data_Products/BUOY_DATA/3HOURLY_DATA/, last access: 20 Jan 2025.
  - Hourly data (after 2016) were obtained from https://iabp.apl.uw.edu/WebData/LEVEL2/, last access: 20 Jan 2025.

A snapshot of the Drift-Aware Python toolbox used to produce the results in this study is available on Zenodo: https://doi.org/10.5281/zenodo.14732875, last access 24 Jan 2025.

Video supplement. The video supplement contains an animated timeseries of DA-SIT maps from 2019–2020.

Appendix A: Validation Datasets Overview

A1 AEM datasets

Table A1 lists the AEM data records for the period 2007-2019, which are used for validation in this study as well as the surveyed regions and used platform.

A2 ULS datasets

Table A2 provides the position of the moorings in the Beaufort Sea and information about the ULS data record periods. They cover the Envisat (A, B, C, D), as well as the CryoSat-2 era (A, B, D).

Author contributions. Original idea of the Drift-Aware approach: RR, TL Design and development of the Drift-Aware algorithm: RR, MB. Sea ice drift data input and interpretation: TL, ED. Sea ice thickness data input and interpretation: SH, SP. Project support: MAK. Discussion of results and conclusions: All. Writing the manuscript: All.

Competing interests. The authors declare that they have no conflict of interest.

Acknowledgements. RR and MB were supported by ESA CCI Sea Ice (CCN-2 to Contract 4000126449/19/I-NB -Sea_Ice_cci), the Fram Centre project "Sustainable Development of the Arctic Ocean" (SUDARCO) (project_ID: 2551323), and the Research Council of Norway project "Thickness of Arctic sea ice Reconstructed by Data assimilation and artificial Intelligence Seamlessly" (TARDIS) (grant 325241).

TL and MAK were supported by ESA CCI Sea Ice (CCN-2 to Contract 4000126449/19/I-NB -Sea_Ice_cci). ED was supported by the EUMETSAT OSI SAF fourth Continuous Development and Operations Phase (CDOP4).

References

Bocquet, M., Fleury, S., Rémy, F., and Piras, F.: Arctic and Antarctic Sea Ice Thickness and Volume Changes From Observations Between 1994 and 2023, Journal of Geophysical Research: Oceans, 129, e2023JC020 848, https://doi.org/https://doi.org/10.1029/2023JC020848, e2023JC020848 2023JC020848, 2024.

Brodzik, M. J., Billingsley, B., Haran, T., Raup, B., and Savoie, M. H.: EASE-Grid 2.0: Incremental but Significant Improvements for Earth-Gridded Data Sets, ISPRS International Journal of Geo-Information, 1, 32–45, https://doi.org/10.3390/ijgi1010032, 2012.

Comiso, J. C., Parkinson, C. L., Gersten, R., and Stock, L.: Accelerated decline in the Arctic sea ice cover, Geophysical Research Letters, 35, https://doi.org/10.1029/2007GL031972, 2008.

Farrell, S. L., Duncan, K., Buckley, E. M., Richter-Menge, J., and Li, R.: Mapping Sea Ice Surface Topography in High Fidelity With ICESat-2, Geophysical Research Letters, 47, e2020GL090 708, https://doi.org/https://doi.org/10.1029/2020GL090708, e2020GL090708 2020GL090708, 2020.

Felden, J., Möller, L., Schindler, U., Huber, R., Schumacher, S., Koppe, R., Diepenbroek, M., and Glöckner, F. O.: PANGAEA - Data Publisher for Earth & Environmental Science, Scientific Data, 10, 347, https://doi.org/10.1038/s41597-023-02269-x, 2023.

Fredensborg Hansen, R. M., Skourup, H., Rinne, E., Høyland, K. V., Landy, J. C., Merkouriadi, I., and Forsberg, R.: Arctic Freeboard and Snow Depth From Near-Coincident CryoSat-2 and ICESat-2 (CRYO2ICE) Observations: A First Examination of Winter Sea Ice During 2020–2022, Earth and Space Science, 11, e2023EA003 313, https://doi.org/https://doi.org/10.1029/2023EA003313, e2023EA003313 2023EA003313, 2024.

Gregory, W., Lawrence, I. R., and Tsamados, M.: A Bayesian approach towards daily pan-Arctic sea ice freeboard estimates from combined CryoSat-2 and Sentinel-3 satellite observations, The Cryosphere, 15, 2857–2871, https://doi.org/10.5194/tc-15-2857-2021, 2021.

Haas, C., Lobach, J., Hendricks, S., Rabenstein, L., and Pfaffling, A.: Helicopter-borne measurements of sea ice thickness, using a small and lightweight, digital EM system, Journal of Applied Geophysics, 67, 234–241, https://doi.org/https://doi.org/10.1016/j.jappgeo.2008.05.005, airborne Geophysics, 2009.

Hansen, E., Gerland, S., Granskog, M. A., Pavlova, O., Renner, A. H. H., Haapala, J., Løyning, T. B., and Tschudi, M.: Thinning of Arctic sea ice observed in Fram Strait: 1990–2011, Journal of Geophysical Research: Oceans, 118, 5202–5221, https://doi.org/https://doi.org/10.1002/jgrc.20393, 2013.

Hendricks, S., Paul, S., and Rinne, E.: ESA Sea Ice Climate Change Initiative (Sea_Ice_cci): Northern hemisphere sea ice thickness from CryoSat-2 on the satellite swath (L2P), v3.0. NERC EDS Centre for Environmental Data Analysis, https://catalogue.ceda.ac.uk/uuid/c6504378f78c4ecd9f839b0434023eff/, 2024a.

Hendricks, S., Paul, S., and Rinne, E.: ESA Sea Ice Climate Change Initiative (Sea_Ice_cci): Northern hemisphere sea ice thickness from Envisat on the satellite swath (L2P), v3.0. NERC EDS Centre for Environmental Data Analysis, https://catalogue.ceda.ac.uk/uuid/92eb2ba942074bec804af6a8b5436bee/, 2024b.

Heorton, H., Tsamados, M., Landy, J., and Holland, P. R.: Observationally constrained estimates of the annual Arctic sea-ice volume budget 2010–2022, Annals of Glaciology, 66, e9, https://doi.org/10.1017/aog.2025.3, 2025.

Howell, S. E. L., Brady, M., and Komarov, A. S.: Generating large-scale sea ice motion from Sentinel-1 and the RADARSAT Constellation Mission using the Environment and Climate Change Canada automated sea ice tracking system, The Cryosphere, 16, 1125–1139, https://doi.org/10.5194/tc-16-1125-2022, 2022.

Kern, M., Cullen, R., Berruti, B., Bouffard, J., Casal, T., Drinkwater, M. R., Gabriele, A., Lecuyot, A., Ludwig, M., Midthassel, R., Navas Traver, I., Parrinello, T., Ressler, G., Andersson, E., Martin-Puig, C., Andersen, O., Bartsch, A., Farrell, S., Fleury, S., Gascoin, S., Guillot, A., Humbert, A., Rinne, E., Shepherd, A., van den Broeke, M. R., and Yackel, J.: The Copernicus Polar Ice and Snow Topography Altimeter (CRISTAL) high-priority candidate mission, The Cryosphere, 14, 2235–2251, https://doi.org/10.5194/tc-14-2235-2020, 2020.

Khvorostovsky, K., Hendricks, S., and Rinne, E.: Surface Properties Linked to Retrieval Uncertainty of Satellite Sea-Ice Thickness with Upward-Looking Sonar Measurements, Remote Sensing, 12, https://doi.org/10.3390/rs12183094, 2020.

Krishfield, R. A., Proshutinsky, A., Tateyama, K., Williams, W. J., Carmack, E. C., McLaughlin, F. A., and Timmermans, M.-L.: Deterioration of perennial sea ice in the Beaufort Gyre from 2003 to 2012 and its impact on the oceanic freshwater cycle, Journal of Geophysical Research: Oceans, 119, 1271–1305, https://doi.org/https://doi.org/10.1002/2013JC008999, 2014.

Kwok, R., Cunningham, G. F., and Pang, S. S.: Fram Strait sea ice outflow, Journal of Geophysical Research: Oceans, 109, https://doi.org/https://doi.org/10.1029/2003JC001785, 2004.

Kwok, R., Spreen, G., and Pang, S.: Arctic sea ice circulation and drift speed: Decadal trends and ocean currents, Journal of Geophysical Research: Oceans, 118, 2408–2425, https://doi.org/https://doi.org/10.1002/jgrc.20191, 2013.

Landrum, L. and Holland, M. M.: Extremes become routine in an emerging new Arctic, Nature Climate Change, 10, 1108–1115, https://doi.org/10.1038/s41558-020-0892-z, 2020.

Lavergne, T. and Down, E.: A climate data record of year-round global sea-ice drift from the EUMETSAT Ocean and Sea Ice Satellite Application Facility (OSI SAF), Earth System Science Data, 15, 5807–5834, https://doi.org/10.5194/essd-15-5807-2023, 2023.

Lavergne, T., Sørensen, A. M., Kern, S., Tonboe, R., Notz, D., Aaboe, S., Bell, L., Dybkjær, G., Eastwood, S., Gabarro, C., Heygster, G., Killie, M. A., Brandt Kreiner, M., Lavelle, J., Saldo, R., Sandven, S., and Pedersen, L. T.: Version 2 of the EUMETSAT OSI SAF and ESA CCI sea-ice concentration climate data records, The Cryosphere, 13, 49–78, https://doi.org/10.5194/tc-13-49-2019, 2019.

Lavergne, T., Piñol Solé, M., Down, E., and Donlon, C.: Towards a swath-to-swath sea-ice drift product for the Copernicus Imaging Microwave Radiometer mission, The Cryosphere, 15, 3681–3698, https://doi.org/10.5194/tc-15-3681-2021, 2021.

Lavergne, T., Kern, S., Aaboe, S., Derby, L., Dybkjaer, G., Garric, G., Heil, P., Hendricks, S., Holfort, J., Howell, S., Key, J., Lieser, J. L., Maksym, T., Maslowski, W., Meier, W., Muñoz-Sabater, J., Nicolas, J., Özsoy, B., Rabe, B., Rack, W., Raphael, M., de Rosnay, P., Smolyanitsky, V., Tietsche, S., Ukita, J., Vichi, M., Wagner, P., Willmes, S., and Zhao, X.: A New Structure for the Sea Ice Essential Climate Variables of the Global Climate Observing System, Bulletin of the American Meteorological Society, 103, E1502 – E1521, https://doi.org/10.1175/BAMS-D-21-0227.1, 2022.

Lavergne, T., Sørensen, A., Tonboe, R., Strong, C., Kreiner, M., Saldo, R., Birkedal, A., Baordo, F., Rusin, J., Aspenes, T., and Eastwood, S.: Monitoring of Sea Ice Concentration, Area, and Extent in the polar regions : 40+ years of data from EUMETSAT OSI SAF and ESA CCI, https://doi.org/10.5281/zenodo.10014535, 2023.

Laxon, S. W., Giles, K. A., Ridout, A. L., Wingham, D. J., Willatt, R., Cullen, R., Kwok, R., Schweiger, A., Zhang, J., Haas, C., Hendricks, S., Krishfield, R., Kurtz, N., Farrell, S., and Davidson, M.: CryoSat-2 estimates of Arctic sea ice thickness and volume, Geophysical Research Letters, 40, 732–737, https://doi.org/https://doi.org/10.1002/grl.50193, 2013.

Lindsay, R. and Schweiger, A.: Arctic sea ice thickness loss determined using subsurface, aircraft, and satellite observations, The Cryosphere, 9, 269–283, https://doi.org/10.5194/tc-9-269-2015, 2015.

Meier, W. N. and Stewart, J. S.: NSIDC Land, Ocean, Coast, Ice, and Sea Ice Region Masks. NSIDC Special Report 25. Boulder CO, USA: National Snow and Ice Data Center, 2023.

OSI-405: OSI SAF Global Low Resolution Sea Ice Drift, OSI-405-c, https://doi.org/10.15770/EUM_SAF_OSI_NRT_2007, 2007.

OSI-450-a: OSI SAF Global Sea Ice Concentration Climate Data Record 1978-2020 (v3.0, 2022), https://doi.org/10.15770/EUM_SAF_OSI_0013, data extracted from ftp://osisaf.met.no: 2002-2020, accessed August 2023, 2022.

OSI-455: OSI SAF Global Low Resolution Sea Ice Drift Data Record 1991-2020 (v1, 2022), https://doi.org/10.15770/EUM_SAF_OSI_0012, data extracted from ftp://osisaf.met.no: 2002-2020, accessed August 2023, 2022.

Paul, S., Hendricks, S., Ricker, R., Kern, S., and Rinne, E.: Empirical parametrization of Envisat freeboard retrieval of Arctic and Antarctic sea ice based on CryoSat-2: progress in the ESA Climate Change Initiative, The Cryosphere, 12, 2437–2460, https://doi.org/10.5194/tc-12-2437-2018, 2018.

Paul, S., Hendricks, S., Rinne, E., and Sallila, H.: CCI+ Sea Ice ECV - Sea Ice Thickness Algorithm Theoretical Basis Document (ATBD), https://doi.org/10.5281/zenodo.10605840, 2024.

Petty, A. A., Kurtz, N. T., Kwok, R., Markus, T., and Neumann, T. A.: Winter Arctic Sea Ice Thickness From ICESat-2 Freeboards, Journal of Geophysical Research: Oceans, 125, e2019JC015 764, https://doi.org/https://doi.org/10.1029/2019JC015764, e2019JC015764 2019JC015764, 2020.

Pfaffling, A., Haas, C., and Reid, J. E.: Direct helicopter EM — Sea-ice thickness inversion assessed with synthetic and field data, GEOPHYSICS, 72, F127–F137, https://doi.org/10.1190/1.2732551, 2007.

Polyakov, I. V., Pnyushkov, A. V., Alkire, M. B., Ashik, I. M., Baumann, T. M., Carmack, E. C., Goszczko, I., Guthrie, J., Ivanov, V. V., Kanzow, T., Krishfield, R., Kwok, R., Sundfjord, A., Morison, J., Rember, R., and Yulin, A.: Greater role for Atlantic inflows on sea-ice loss in the Eurasian Basin of the Arctic Ocean, Science, 356, 285–291, https://doi.org/10.1126/science.aai8204, 2017.

Ricker, R., Hendricks, S., Helm, V., Skourup, H., and Davidson, M.: Sensitivity of CryoSat-2 Arctic sea-ice freeboard and thickness on radar-waveform interpretation, The Cryosphere, 8, 1607–1622, https://doi.org/10.5194/tc-8-1607-2014, 2014.

Ricker, R., Hendricks, S., Kaleschke, L., Tian-Kunze, X., King, J., and Haas, C.: A weekly Arctic sea-ice thickness data record from merged CryoSat-2 and SMOS satellite data, The Cryosphere, 11, 1607–1623, https://doi.org/10.5194/tc-11-1607-2017, 2017.

Ricker, R., Girard-Ardhuin, F., Krumpen, T., and Lique, C.: Satellite-derived sea ice export and its impact on Arctic ice mass balance, The Cryosphere, 12, 3017–3032, https://doi.org/10.5194/tc-12-3017-2018, 2018.

Ricker, R., Kauker, F., Schweiger, A., Hendricks, S., Zhang, J., and Paul, S.: Evidence for an Increasing Role of Ocean Heat in Arctic Winter Sea Ice Growth, Journal of Climate, 34, 5215 – 5227, https://doi.org/10.1175/JCLI-D-20-0848.1, 2021.

Ricker, R., Fons, S., Jutila, A., Hutter, N., Duncan, K., Farrell, S. L., Kurtz, N. T., and Fredensborg Hansen, R. M.: Linking scales of sea ice surface topography: evaluation of ICESat-2 measurements with coincident helicopter laser scanning during MOSAiC, The Cryosphere, 17, 1411–1429, https://doi.org/10.5194/tc-17-1411-2023, 2023.

Sallila, H., Farrell, S. L., McCurry, J., and Rinne, E.: Assessment of contemporary satellite sea ice thickness products for Arctic sea ice, The Cryosphere, 13, 1187–1213, https://doi.org/10.5194/tc-13-1187-2019, 2019.

Selyuzhenok, V., Bashmachnikov, I., Ricker, R., Vesman, A., and Bobylev, L.: Sea ice volume variability and water temperature in the Greenland Sea, The Cryosphere, 14, 477–495, https://doi.org/10.5194/tc-14-477-2020, 2020.

Spreen, G., Kwok, R., and Menemenlis, D.: Trends in Arctic sea ice drift and role of wind forcing: 1992–2009, Geophysical Research Letters, 38, https://doi.org/https://doi.org/10.1029/2011GL048970, 2011.

Sumata, H., Lavergne, T., Girard-Ardhuin, F., Kimura, N., Tschudi, M. A., Kauker, F., Karcher, M., and Gerdes, R.: An intercomparison of Arctic ice drift products to deduce uncertainty estimates, Journal of Geophysical Research: Oceans, 119, 4887–4921, https://doi.org/https://doi.org/10.1002/2013JC009724, 2014.

Tian-Kunze, X., Kaleschke, L., Maaß, N., Mäkynen, M., Serra, N., Drusch, M., and Krumpen, T.: SMOS-derived thin sea ice thickness: algorithm baseline, product specifications and initial verification, The Cryosphere, 8, 997–1018, https://doi.org/10.5194/tc-8-997-2014, 2014.

Tilling, R. L., Ridout, A., and Shepherd, A.: Estimating Arctic sea ice thickness and volume using CryoSat-2 radar altimeter data, Advances in Space Research, 62, 1203–1225, https://doi.org/https://doi.org/10.1016/j.asr.2017.10.051, the CryoSat Satellite Altimetry Mission: Eight Years of Scientific Exploitation, 2018.

Virtanen, P., Gommers, R., Oliphant, T. E., Haberland, M., Reddy, T., Cournapeau, D., Burovski, E., Peterson, P., Weckesser, W., Bright, J., van der Walt, S. J., Brett, M., Wilson, J., Millman, K. J., Mayorov, N., Nelson, A. R. J., Jones, E., Kern, R., Larson, E., Carey, C. J., İlhan Polat, Feng, Y., Moore, E. W., VanderPlas, J., Laxalde, D., Perktold, J., Cimrman, R., Henriksen, I., Quintero, E. A., Harris, C. R., Archibald, A. M., Ribeiro, A. H., Pedregosa, F., van Mulbregt, P., Vijaykumar, A., Bardelli, A. P., Rothberg, A., Hilboll, A., Kloeckner, A., Scopatz, A., Lee, A., Rokem, A., Woods, C. N., Fulton, C., Masson, C., Häggström, C., Fitzgerald, C., Nicholson, D. A., Hagen, D. R., Pasechnik, D. V., Olivetti, E., Martin, E., Wieser, E., Silva, F., Lenders, F., Wilhelm, F., Young, G., Price, G. A., Ingold, G.-L., Allen, G. E., Lee, G. R., Audren, H., Probst, I., Dietrich, J. P., Silterra, J., Webber, J. T., Slavič, J., Nothman, J., Buchner, J., Kulick, J., Schönberger, J. L., de Miranda Cardoso, J. V., Reimer, J., Harrington, J., Rodríguez, J. L. C., Nunez-Iglesias, J., Kuczynski, J., Tritz, K., Thoma, M., Newville, M., Kümmerer, M., Bolingbroke, M., Tartre, M., Pak, M., Smith, N. J., Nowaczyk, N., Shebanov, N., Pavlyk, O., Brodtkorb, P. A., Lee, P., McGibbon, R. T., Feldbauer, R., Lewis, S., Tygier, S., Sievert, S., Vigna, S., Peterson, S., More, S., Pudlik, T., Oshima, T., Pingel, T. J., Robitaille, T. P., Spura, T., Jones, T. R., Cera, T., Leslie, T., Zito, T., Krauss, T., Upadhyay, U., Halchenko, Y. O., Vázquez-Baeza, Y., and Contributors, S. .: SciPy 1.0: Fundamental Algorithms for Scientific Computing in Python, Nature Methods, 17, 261–272, https://doi.org/10.1038/s41592-019-0686-2, 2020.

Zhang, F., Pang, X., Lei, R., Zhai, M., Zhao, X., and Cai, Q.: Arctic sea ice motion change and response to atmospheric forcing between 1979 and 2019, International Journal of Climatology, 42, 1854–1876, https://doi.org/https://doi.org/10.1002/joc.7340, 2022.

Table A1. AEM data record overview used in this study. Data are only considered if they match with the respective satellite product coverage.

Campaign Name	Period	Region	Aircraft Type
SEDNA	05.04.2007 - 13.04.2007	Beaufort Sea/ Chukchi Sea	Helicopter EM
SIZONet	12.04.2008 - 14.04.2008	Beaufort Sea/ Chukchi Sea	Helicopter EM
PAMARCMIP	05.04.2009 - 26.04.2009	Beaufort Sea/ Chukchi Sea/ Fram Strait	Fixed-wing aircraft EM
SIZONet	09.04.2010 - 12.04.2010	Beaufort Sea/ Chukchi Sea	Helicopter EM
PAMARCMIP	31.03.2011 - 28.04.2011	Beaufort Sea/ Chukchi Sea/ Lincoln Sea/ Fram Strait	Fixed-wing aircraft EM
PAMARCMIP	03.04.2012 - 05.04.2012	Beaufort Sea/ Chukchi Sea/ Lincoln Sea	Fixed-wing aircraft EM
SIZONet	07.04.2012 - 09.04.2012	Beaufort Sea	Helicopter EM
SIZONet	30.03.2013 - 03.04.2013	Beaufort Sea	Helicopter EM
SIZONet	04.04.2014 - 05.04.2014	Beaufort Sea/ Chukchi Sea	Helicopter EM
PAMARCMIP	07.04.2015 - 23.04.2015	Beaufort Sea/ Chukchi Sea/ Lincoln Sea	Fixed-wing aircraft EM
PAMARCMIP	21.03.2017 - 08.04.2017	Arctic Ocean/ Fram Strait/ Beaufort Sea/ Chukchi Sea/ Lincoln Sea	Fixed-wing aircraft EM
ICEBIRD	01.04.2019 - 10.04.2019	Beaufort Sea/ Chukchi Sea/ Lincoln Sea	Fixed-wing aircraft EM

Table A2. Mooring sites with ULS measurement periods used in this study.

Mooring Site	ULS Record Periods	Location
A	08/2003 – 04/2020	150.0°W 75.0°N
B	08/2003 – 09/2009	150.0°W 80.0°N
	10/2010 – 04/2020	
C	08/2003 – 07/2008	140.0°W 77.0°N
D	09/2006 – 04/2020	140.0°W 74.0°N